Densification of cathode/electrolyte interphase to enhance reversibility of $LiCoO_2$ at 4.65 V

Hengyu Ren,[1] *Jiaxuan Hu,*[1] *Haocheng Ji,*[2] *Yuxiang Huang,*[1] *Wenguang Zhao,*[1] *Weiyuan Huang,*[3] *Xiaohu Wang,*[1] *Haocong Yi,*[1] *Yongli Song,*[4] *Jiajie Liu,*[1] *Tongchao Liu,*[3] *Ming Liu,*[5] *Qinghe Zhao,**[*,1] *Feng Pan**[*,1]

H. Ren, J. Hu, Y. Huang, W. Zhao, X. Wang, H. Yi, J. Liu, Q. Zhao,* F. Pan*

1 School of Advanced Materials, Peking University Shenzhen Graduate School, Peking University, Shenzhen, Guangdong province, 518055, China

E-mail: zhaoqh@pku.edu.cn; panfeng@pkusz.edu.cn

H. Ji

2 Tsinghua-Berkeley Shenzhen Institute & Tsinghua Shenzhen International Graduate School, Tsinghua University, Shenzhen, Guangdong province, 518055, China

W. Huang, T. Liu

3 Chemical Sciences and Engineering Division, Argonne National Laboratory, Lemont, IL, 60439, USA

Y. Song

4 School of Energy and Power Engineering, Jiangsu University, Zhenjiang, Jiangsu province, 212013, China

M. Liu

5 Institute of Materials Research, Tsinghua Shenzhen International Graduate School, Tsinghua University, Shenzhen, Guangdong province, 518055, China

Keywords: High-voltage $LiCoO_2$, Cathode/electrolyte interphase, Zr-O deposits, Interface reaction, Li-ion batteries

Abstract

For $LiCoO_2$ (LCO) operated beyond 4.55 V (vs. Li/Li^+), it usually suffers from severe surface degradation. Constructing a robust cathode/electrolyte interphase (CEI) is effective to alleviate the above issues, however, the correlated mechanisms still remain vague. Herein, a progressively reinforced CEI is realized via constructing Zr-O deposits (ZrO_2 and Li_2ZrO_3) on LCO surface (i.e., Z-LCO). Upon cycle, these Zr-O deposits can promote the decomposition of $LiPF_6$, and progressively convert to the highly dispersed Zr-O-F species. In particular, the chemical reaction between LiF and Zr-O-F species further leads to the densification of CEI, which greatly reinforces its toughness and conductivity. Combining the robust CEI and thin surface rock-salt layer of Z-LCO, several benefits are achieved, including stabilizing the surface lattice oxygen, facilitating the interface Li^+ transport kinetics, and enhancing the reversibility of O3/H1-3 phase transition, etc. As a result, the Z-LCO||Li cells exhibit a high capacity retention of 84.2% after 1000 cycles in 3-4.65 V, 80.9% after 1500 cycles in 3-4.6 V, and a high rate capacity of 160 mA h g^{-1} at 16 C (1 C = 200 mA g^{-1}). This work provides a new insight for developing advanced LCO cathodes.

1 Introduction

Currently, $LiCoO_2$ (LCO) cathodes, with a typical layered structure for the storage of Li^+ ions, has been utilized in many applications, mainly due to its high energy density and long cycle life.[1-3] In order to achieve higher energy density, lots of attempts have been performed to increase its charging cut-off voltage to beyond 4.6 V (vs. Li/Li^+), thus more capacity can be released. However, when operated above 4.6 V, the harsh high-voltage cycle conditions can induce serious issues of surface Co/O loss and structure degradation, which blocks the practical usage of high-voltage LCO.[1-2, 4]

The surface degradation issues originate from the detrimental interface reactions. For instance, some solvents in electrolytes, such as the ethylene carbonate (EC), tend to be dehydrogenated/ oxidized in the LCO/electrolyte interface upon charging, and produces some H^+/H_2O to promote the hydrolysis of PF_6^- anions, causing the formation of corrosive species, including HF, HPO_2F_2, etc., and leading to Co dissolution and O loss from LCO surface.[5-7] Besides, the decomposition of solvents can further cause the formation of deteriorated cathode/electrolyte interphase (CEI), which is enriched with organic species, and shows a porous character, or a poor protectiveness on LCO surface.[8-9] Meanwhile, beyond 4.6 V, the LCO surface further suffers from the significant oxidation of lattice oxygen, which releases in form of O_2 at high voltage, and aggravates more interface side reactions.[4, 10] Both the O release and Co dissolution contribute to the surface degradation, causing the obvious blockage for Li^+ transport across the interface and near-surface region of LCO.

To alleviate the above issues, the interface reactions between LCO and electrolyte must be regulated. The strategies of regulating interface reactions includes two aspects, i.e., electrolyte tuning and/or surface modulation. From the perspective of electrolyte tuning, the methods including applying fluorinated solvents, utilizing high-concentration electrolytes or electrolyte additives, etc., are effective to optimize the mechanical properties and conductivity of CEI. The obtained CEI are enriched in the inorganic species, such as LiF, Li_3PO_4 or LiB_xO_y, etc., mainly deriving from the anions' decomposition.[11-15] From the perspective of surface modulation, generally, mitigating the direct contact between surface Co^{4+}/O^{n-} ($0<n<2$) and electrolyte, reducing the surface oxidation activity via substituting the lattice Co/O are the main strategies reported by the previous studies.[2, 16] Notably, more attention has been paid to interface reactions induced by surface structure. For example, applying the surface spinel layer can modify the anion enrichment in the inner Helmholtz layer, promoting the formation of protective LiF-rich CEI on LCO surface.[17] Besides, coating some metal oxides on surface of cathodes, such as ZrO_2, Al_2O_3, MgO, etc., can stabilize the surface structure and produce metal fluorides upon cycle, but the enlarged surface impedance and uneven distribution of these metal oxides limit the performance of the cathodes.[18-22] Thus, to achieve outstanding cycle stability of LCO upon harsh conditions, taking account of the regulation of interface reactions is of great significance.

Herein, the interface reactions of Z-LCO are regulated by the surface Zr-O deposits (ZrO_2 and Li_2ZrO_3) and a thin surface rocksalt (RS) layer. Comprehensive characterizations are performed to reveal the optimization mechanism. Upon cycle, the surface Zr-O deposits, can promote the decomposition of $LiPF_6$, producing large amounts of $LiF/Li_xPF_yO_z$, and progressively convert to the highly dispersed Zr-O-F species. More importantly, accompanying with the fluorination of Zr-O deposits, the CEI layer gradually densifies upon cycle, which greatly reinforces the toughness and conductivity of CEI enriching with the LiF, $Li_xPF_yO_z$ and Zr-F (ZrF_4 and Li_2ZrF_6) inorganic species. This progressively densified CEI and surface RS layer of Z-LCO facilitate the interface Li^+ transport kinetics, and ensure an enhanced and more reversible O3/H1-3 phase transition. As a result, Z-LCO||Li cells demonstrate superior cell performances, with a high capacity retention of 84.2% after 1000 cycles in 3-4.65 V, 80.9% after 1500 cycles in 3-4.6 V, and a high rate capacity of 160 mA h g^{-1} at 16 C (1 C = 200 mA g^{-1}), which is among the best reported performances for high voltage LCO cathodes.

2 Results and Discussion

2.1 Synthesis of the $LiCoO_2$ with Zr-O deposits

In this work, we apply the $ZrO(NO_3)_2$ and NH_4F as Zr/F sources, and use a simple wet-coating process followed by a medium-temperature calcination to obtain the Z-LCO. Upon synthesis, the bare LCO is firstly mixed with the aqueous solution containing $LiNO_3$, $ZrO(NO_3)_2$ and NH_4F salts, then the mixtures are stirred for 1 h at 60°C, to make sure the uniform precipitation of Zr/F species on surface of LCO (**Figure S1, Supporting Information**), and the powders are calcinated at 700°C for 6 h in different atmosphere to yield the final product. As shown in scanning electron microscopy (SEM) images (**Figure S2, Supporting Information**), the variation of calcination atmospheres can greatly affect the morphology of the coated LCO, in which, the coated LCO annealed in air and argon atmosphere are named as Z-LCO and Z-LCO-Ar, respectively.

In **Figure 1a, Figure S3 (Supporting Information)** and **Table S1-3 (Supporting Information)**, the X-ray diffraction (XRD) patterns and Rietveld refinements of Z-LCO, Z-LCO-Ar and LCO are well indexed to the typical layered α-$NaFeO_2$ structure with a space group of *R-3m*, indicating that the surface coating exhibits slight influence on the bulk structure of LCO. The high-resolution transmission electron microscopy (HRTEM) is further applied to analyze the surface structure of LCO. In **Figure S4 (Supporting Information)**, the pristine LCO shows a perfect layered structure with a smooth surface. For Z-LCO, the abundant Zr-O deposits are homogeneously coated on the surface (**Figure 1b**), and energy dispersive spectrometer (EDS) mapping results show the enrichment of Zr on surface of Z-LCO (**Figure S5, Supporting Information**). The cross-sectional structure is further characterized to determine the existence of Zr element on surface of Z-LCO (**Figure 1c**). There are three layers on surface of Z-LCO, i.e., the outermost surface Zr-O deposits, the surface RS layer with a thickness of 5 nm, and the bulk layered structure. The Zr-O deposits are identified as ZrO_2 and Li_2ZrO_3 species (**Figure S6, Supporting Information**). For Z-LCO-Ar, the Zr-O deposits are sparsely and inhomogeneously distributed on the outermost surface, and are composed of the ZrO_2 and Li_2ZrO_3 with significant differences in particle size (**Figure S7, Supporting Information**). In argon atmosphere, the Zr/F elements are more inclined to diffuse into the near-surface region of LCO, and promote the formation of thick surface RS layer (thickness of about 10-15 nm), as confirmed by EDS mapping/line scanning results and in-depth F 1s X-ray photoelectron spectroscopy (XPS) results (**Figure S8, Supporting Information**) and HRTEM images of Z-LCO-Ar. (**Figure S9, Supporting Information**).

XPS measurements are further performed to confirm the influence of calcination atmosphere on surface structure of Z-LCO-Ar and Z-LCO. **Figure S10 (Supporting Information)** shows the XPS results of ZrO_2 and ZrF_4 standard samples, in which the ZrF_4 presents the $Zr_{3d5/2}$ and $Zr_{3d3/2}$ peaks at 188.2 and 185.8 eV, respectively, and the ZrO_2 presents the $Zr_{3d5/2}$ and $Zr_{3d3/2}$ peaks at 182.2 and 184.6 eV, respectively, indicating that the binding energy of Zr-F bonds is higher than that of the Zr-O bonds.[23] **Figure 1d** shows the in-depth Zr 3d XPS analyses of Z-LCO. As observed, the outermost surface Zr-O deposits contains the Zr-O and Zr-O-F, corresponding to the ZrO_2/Li_2ZrO_3 and the fluorinated $ZrO_xF_y/Li_2ZrO_xF_y$ species, respectively.[23-24] As etching up to 20 s, new peaks locating at 181.1 and 183.6 eV appear, which corresponds to the existence of oxygen-deficient ZrO_{2-x} species in surface of Z-LCO. That is to say, the surface RS layer of Z-LCO presents an oxygen-deficient feature, which benefits for the enhanced rate performance.[24] Similar to Z-LCO, the surface of Z-LCO-Ar also contains the Zr-O, Zr-O-F and oxygen-deficient $Zr-O_x$ species (**Figure S11, Supporting Information**). Due to the sparsely distributed surface deposits, these Zr-containing species mainly refer to the components of thick RS phase.

Figure 1e and Figure S12 (Supporting Information) show the Raman spectra results, and all samples exhibit two characteristic peaks at about 480 cm^{-1} and 590 cm^{-1}, corresponding to the lattice vibration of O-Co-O bending mode (E_g) and Co-O stretching mode (A_{1g}), respectively. Comparing with LCO, the E_g and A_{1g} modes of Z-LCO and Z-LCO-Ar shift toward to lower wave numbers, showing an obvious increase in the *c*-axis lattice parameter due to the trace doping of Zr/F elements in the surface region (**Table S1-3, Supporting Information**).[25] Meanwhile, new Raman peaks at about 190 cm^{-1} and 670 cm^{-1} rise for Z-LCO, corresponding to the uniformly distribution of ZrO_2 and RS layer, while for Z-LCO-Ar, only the Raman peak of RS layer exists.[8, 26]

To investigate the interface interaction, soft X-ray absorption spectroscopy (sXAS) of O K-edge spectra using TEY mode is also applied. In **Figure 1f**, the peak locating at the photon energy of 530.5 eV corresponds to the hybridization of Co^{3+} (e^*_g)-O 2p, and the peaks at the photon energy of 531.0 eV and 532.5 eV correspond to the low valence states of Co in surface RS region and the hybridization of Zr^{4+} (e^*_g)-O 2p of the outermost Zr-O deposits, respectively.[8, 10, 27-29] Meanwhile, the broader and higher peaks locating within the photon energies of 535–545 eV further exhibit the excited electron localization effect, implying the stabilized surface lattice oxygen of Z-LCO.[29]

Thus, we reveal the different features of Z-LCO and Z-LCO-Ar, as coated and calcinated in air and argon atmospheres, respectively. In air atmosphere, the outermost surface of Z-LCO contains ZrO_2, Li_2ZrO_3 and the correlated Zr-O-F species, and a thin surface RS layer composing of Li-Co-O-Zr-F is constructed, leading to the reinforced lattice oxygen stabilization. In argon atmosphere, the Zr/F elements are inclined to diffuse into the surface of Z-LCO-Ar, and promote to form a thick RS layer composing of Li-Co-O-Zr-F solid solution. The surface modification affects greatly on the cell performances of Z-LCO and Z-LCO-Ar, as discussed subsequently.

2.2 Cell performances

To evaluate the surface optimization of Z-LCO-Ar and Z-LCO, both the LCO||Li cells and LCO||graphite cells are assembled and tested. In **Figure 2a**, the Z-LCO||Li cell exhibits a high discharge capacity (218.2 mA h g^{-1}) and a high initial Coulombic efficiency (ICE) (95.0%) within the voltage of 3-4.6 V, while for Z-LCO-Ar||Li and LCO||Li cells (**Figure S13,**

Supporting Information), they exhibit the relatively lower discharge capacity and lower ICE values. The Z-LCO-Ar||Li cell shows a discharge capacity of 215.9 mA h g^{-1}, and ICE of 92.0%, and the LCO||Li cell shows a discharge capacity of 216.0 mA h g^{-1}, and ICE of 93.2%, respectively.

Cyclic voltammetry (CV) curves (**Figure 2b; Figure S14, Supporting Information**) illustrate that, the surface modulation presents a significant depolarization effect, i.e., the CV curves for Z-LCO||Li and Z-LCO-Ar||Li cells show the much smaller half-peak width and voltage hysteresis of CV peaks than that of LCO||Li cell, and the Z-LCO||Li cell exhibits the the most obvious depolarization effect, or the best Li^+ transport kinetics.[30] This can be further confirmed by the galvanostatic intermittent titration technique (GITT) (**Figure 2c; Figure S15, Supporting Information**). As observed, upon cycle, the Li^+ diffusion coefficients decrease gradually in a order of Z-LCO > Z-LCO-Ar > LCO, indicating the facilitated Li^+ transport kinetics of Z-LCO due to the surface Zr-O deposits and RS phase. Thus, the Z-LCO||Li cell presents both the promoted rate performance and enhanced cycle stability.

The enhanced cycle stability and promoted rate performance of Z-LCO are further evaluated within the voltage of 3-4.6 V and 3-4.65 V. In the voltage range of 3-4.6 V, as shown in **Figure 2d**, the Z-LCO||Li cell exhibits an ultrahigh cycle stability with a high initial discharge capacity of 203.0 mA h g^{-1} and high capacity retention of 91.1% after 500 cycles at 1 C (1 C = 200 mA g^{-1}). When operated at higher rate currents of 2, 4, 8 and 16 C, the discharge capacities of Z-LCO||Li cell are 195.7, 187.1, 175.5 and 160.0 mA h g^{-1}, respectively, which are obviously better than Z-LCO-Ar||Li and LCO||Li cells (**Figure S16, Supporting Information**). The corresponding charge/discharge curves are shown in **Figure S17 (Supporting Information)**. Meanwhile, the Z-LCO||Li cell also show the enhanced cycle performance at high rate operation (**Figure 2f; Figure S18, Supporting Information**), which exhibits a high capacity retention of 85.0% after 1500 cycles at 2 C (with initial discharge capacity of 195.7 mA h g^{-1}), 80.9% after 1500 cycles at 5 C (with initial discharge capacity of 188.6 mA h g^{-1}) and 82.4% after 1500 cycles at 10 C (with initial discharge capacity of 170.0 mA h g^{-1}), which is much better than that of Z-LCO-Ar||Li cell, and obviously superior to that of LCO||Li cell. In the voltage range of 3-4.65 V, the Z-LCO||Li cell maintains the superior cell performance (**Figure S19, Supporting Information**), showing a capacity retention of 84.2% after 1000 cycles at 5 C (with initial discharge capacity of 191.7 mA h g^{-1}). In **Figure 2g and Table S4 (Supporting Information)**, we also list the cell performance comparison of different kinds of surface modifications of LCO, which show that Z-LCO has a competitive performance upon high voltage operations (≥ 4.6 V).

By comparing the charge-discharge curves of Z-LCO||Li, Z-LCO-Ar||Li, and LCO||Li cells during cycling (**Figure S17-19, Supporting Information**), the results show the obviously reduced capacity decay and voltage decay of Z-LCO||Li cells, indicating the enhanced structure stability of Z-LCO due to the surface modulation. Besides, the cycle performances of cells at 45 °C are also performed to evaluate their high-temperature durability. In **Figure S20 (Supporting Information)**, the cycle stability, rate capacity and floating durability of cells are tested and compared, and the order of performances from superior to inferior is Z-LCO||Li cell > LCO||Li cell > Z-LCO-Ar||Li cell. As noted, the Z-LCO-Ar||Li cell shows a even worse performance than the LCO||Li cell, demonstrating that the thick surface RS layer is incapable for high-temperature applications. Thus, the applicability of surface modification is a significant issue that must be carefully handled. Moreover, the Z-LCO||Li cells with high cathode loading (>10 mg cm^{-2}) display similar electrochemical performances, the Z-LCO||graphite cell also demonstrates remarkable stability with a high capacity retention of 94% after 500 cycles in 3-4.55 V at 1 C (**Figure S21, Supporting Information**).

2.3 Reduced interface side reactions

Upon cycle at 4.6 V, the highly oxidative Co^{4+}/O^{n-} ($0<n<2$) on LCO surface usually induce severe interface reactions, leading to the Co/O loss from surface Co-O lattice and surface structure degradation. For Z-LCO, the surface modification can significantly reduce the detrimental interface side reactions. In **Figure 3a,b**, the *in-situ* differential electrochemical mass spectrometry (DEMS) is applied to detect the reactions in both LCO/electrolyte and Z-LCO/electrolyte interfaces. As observed, in the initial 2 cycles, the release of gases, including CO_2, CO and O_2, is much lesser from Z-LCO||Li cell than that from LCO||Li cell, demonstrating that, the surface modulation on surface of Z-LCO can lower the surface oxygen activity and suppress the electrolyte decomposition.[19] The surface Zr-O deposits may act as a physical barrier between Z-LCO and electrolyte, and the strength of Co-O bonds is significantly enhanced due to the existence of surface RS phase with Zr/F doping (i.e., Li-Co-O-Zr-F). Therefore, the lattice O on surface of Z-LCO is stabilized, leading to the reduced interface side reactions, as well as the reduced gas release.

We further conduct the sXAS of O K-edge spectra using TEY mode to analyze the difference of interface reactions between LCO and Z-LCO. There are 5 kinds of states of electrodes, including the pristine states, and fully charged/discharged states in the 1st and 10th cycles. In **Figure 3c**, upon the 1st charging to 4.6 V, the peaks locating at photon energy of 529 eV and 527 eV emerge, which indicates the formation of hybridization of Co^{4+} (e^*_g)-O 2p and Co^{4+} (t_{2g})-O 2p, representing a highly oxidative character of LCO surface (**Figure 3a**). [10, 31] Due to this highly oxidative character, the electrolyte solvents decompose dramatically, and form plenty of carbonyle-cotaining products and Li_2CO_3, corresponding to the peaks locating at photon energy of 532 eV, and at photon energies of 533 eV and 538 eV, respectively.[32] Meanwhile, due to the serious O loss, CoO/Co_3O_4 form on the LCO surface, and the characteristic sXAS peaks locate at 531, 535, and 538 eV.[32-33] Upon the 10th charging to 4.6 V, the above interface reactions occur constantly, and form plenty of by-products covering on the surface of LCO, leading to the deteriorated Li^+ transport kinetics across the surface of LCO. In contrast, for Z-LCO, no signals of electrolyte oxidation products and CoO/Co_3O_4 are detected, indicating both the reduced interface side reactions and the well-maintained surface structure (**Figure 3d**). Upon the 1st and 10th charging to 4.6 V, weak Co^{4+}-O 2p signals are detected, and the signals of RS layer/ Zr^{4+} (e^*_g)-O 2p exist persistently, indicating the stabilized surface structure and the reduced surface oxidation activity. It is noted that, from the pristine to the 10th cycle, the peak intensity of surface RS phase decreases gradually, while the peak intensity of Zr-O maintains well, indicating the progressive formation of robust CEI on surface of Z-LCO.

2.4 Mechanism of Zr-O deposits inducing progressively densified CEI

As discussed above, the interface reaction is reduced due to the surface Zr-O deposits and RS phase of Z-LCO, which promotes the formation of robust CEI. To further clarify the progressively reinforced CEI of Z-LCO, various characterizations are conducted, including the cryogenic transmission electron microscopy (cryo-TEM), atomic force microscope (AFM), XPS and time-of-flight secondary ion mass spectrometry (TOF-SIMS). As shown in **Figure 4a-f**, the character and composition of CEI layers on surface of Z-LCO at the 20th and 100th cycles are analyzed under the assistance of cryo-TEM and FFT.[34-35] At the 20th cycle, the CEI of Z-LCO enriches with large amount of deposits, composing of LiF and Zr-O species, and with a thickness of about 100 nm, as confirmed by the cryo-TEM and FFT results in different particles (**Figure 4a-c; Figure S22, Supporting Information**).[36-37] As it advances to the 100th cycle, the CEI becomes more uniform and compact, with a thickness of about 30 nm, and the FFT results indicate that, in addition to the LiF and Zr-O species, a certain amount of Zr-F species (Li_2ZrF_6 and ZrF_4) appear in the CEI layer (**Figure 4d-f; Figure S23-24, Supporting Information**). Furthermore, after 500th cycles, it is clearly that CEI layer becomes much denser without obvious LiF deposits existing, while large amount of Li_2ZrF_6 exist in the CEI (**Figure S25-26, Supporting Information**). Thus, according to the cryo-TEM results, the CEI of Z-LCO goes through an progressive densification process, accompanying with the evolution of compositions. However, for Z-LCO-Ar and LCO, the CEI layers exhibit heterogeneous and loose features, composing of the amorphous species, and the surface regions are obviously damaged due to the severe interface side reactions (**Figure S27-28, Supporting Information**).

AFM is further applied to characterize the mechanical properties of CEI layers on both Z-LCO and LCO (**Figure 4g,h; Figure S29-30, Supporting Information**). As observed, after 100 cycles, the Young's modulus of CEI on Z-LCO surface is evenly distributed and the average value reaches a high value of 15.73 Gpa, while for LCO, the average value of Young's modulus of CEI is just 2.56 Gpa, indicating the obviously reinforced mechanical strength of CEI due to the surface modulation of Z-LCO.[13] Besides, the CEI evolution of Z-LCO can be further characterized by the electrochemical impedance spectroscopy (EIS) (**Figure S31a-e, Supporting Information**). The EIS plots can be fitted and resolved to obtain two significant parameters, i.e., the charge transfer resistance (R_{ct}) referring to the property of surface structure, and the surface film resistance (R_{sf}) referring to property of CEI on the LCO cathode and solid electrolyte interphase (SEI) on the Li anode.[38] However, the difference of R_{sf} in **Figure S31** (**Supporting Information**) mainly comes from the evolution of CEI, which can be confirmed by the corresponding distribution of relaxation time (DRT) curve (**Figure S32, Supporting**

Information).[39] As shown in **Figure 4i**, the R_{sf} of Z-LCO decreases gradually in 500 cycles, showing a gradually enhanced Li^+ transport kinetics across the CEI, which is consistent with the CEI evolution of cryo-TEM results. In contrast, the R_{sf} values of LCO and Z-LCO-Ar are obviously higher than Z-LCO (**Figure S31f, Supporting Information**), indicating the deteriorated Li^+ transport kinetics across the CEI layers. **Figure S32 (Supporting Information)** exhibits the DRT curves extracted by Fourier transform of EIS results after different cycles, for Z-LCO, the peaks of R_{CEI} show decreased signal intensity and shift to lower relaxation time τ, suggesting the enhanced Li^+ transport kinetics through the CEI, while for Z-LCO-Ar and LCO, the results reverse and show sluggish Li^+ transport kinetics.[40-41] Due to the optimized CEI, the surface structure of Z-LCO is well-protected upon cycle, as reflected in **Figure S31g (Supporting Information)**, the R_{ct} values of Z-LCO are obviously lower than that of LCO and Z-LCO-Ar in long-term cycles, which will be discussed subsequently.

Besides, by fitting the R_{sf} values of Z-LCO||Li and LCO||Li cells at temperatures from 30 to 55 °C with Arrhenius equation (**Figure S33, Supporting Information**), the activation energy barriers (E_a) of Li^+ diffusion across the surface film are calculated.[42] For LCO, the values of E_a are 11.1 and 55.8 kJ mol^{-1} at the 20th and 200th cycles, indicating the gradually increased E_a and enlarged interface impedance. While for Z-LCO, it shows the values of E_a of 52.9 and 6.9 kJ mol^{-1} at the 20th and 200th cycles, respectively, showing the progressively promoted Li^+ transport kinetics across the CEI of Z-LCO combined with the DRT results above.

XPS is further applied to characterize the chemical compositions of CEI of Z-LCO and LCO at the 20th, 100th and 500th cycle. **Figure 5a** shows the evolution of F 1s peaks, indicating that relative amount of LiF decreases, while the relative amount of $Li_xPO_yF_z$ and Zr-F increase upon cycle, which is different from the CEI of LCO, i.e., the LiF and $Li_xPO_yF_z$ products accumulate on the surface upon cycle (**Figure S34, Supporting Information**). In **Figure 5b**, new peaks of $Zr_{3d5/2}$ and $Zr_{3d3/2}$ locating at binding energies of 183.9 and 186.3 eV appear upon cycle, which correspond to the newly formed zirconium fluoride (Zr-O-F-1) species. The Zr-O-F-1 species exhibit higher fluorine degree comparing to the Zr-O-F species in pristine Z-LCO. By calculating the peak area of different species in Zr 3d XPS results, including Zr-O, Zr-O-F, and Zr-O-F-1, it can be acknowledged that the average amount of zirconium fluoride in CEI of Z-LCO increases obviously in 500 cycles (**Figure 5c**).

The spatial distribution of species in CEI of Z-LCO after 100th cycles is further characterized by TOF-SIMS. **Figure 5d** displays the uniform spatial distribution of the ZrF^+ species, which shows higher concentration than that of ZrO^+. **Figure 5e and Figure S35-36 (Supporting Information)** show the variations of species in CEI of Z-LCO and LCO from surface to interior at the 100th cycle. It is noted that, the ZrF^+ species exist throughout the CEI of Z-LCO, accompanying with plenty of LiF_2^-, PO_2^-, $PO_2F_2^-$, and PO_3^- species and fewer C_2HO^- organic component, suggesting that the surface Zr-O deposits can inhibit the decomposition of solvents in Z-LCO/electrolyte interface, and promote the formation of robust CEI. The obtained CEI is uniform, dense, and inorganic-rich, which benefits a lot on the surface stabilization of Z-LCO. As for LCO, the CEI presents a high content of CoF_2^+ species, demonstrating the obvious HF corrosion on LCO surface. The HF corrosion induced Co dissolution can be further confirmed by the XPS results of the cycled Li anode and coupled plasma-optical emission spectroscopy (ICP-OES) results of solutions with dissolved Li anodes, which show obvious Co signals after cycles (**Figure S37, Supporting Information**). Since there is no surface coating on the pristine LCO surface, upon charging, the electrolyte can react directly with the highly oxidative Co^{4+}/O^{n-}, causing the decomposition and dehydrogenation of solvents. As a result, some H^+/H_2O is produced to aggravate the hydrolysis of $LiPF_6$ salt, generating plenty of corrosive species, such as HF, HPO_2F_2, etc., and causing Co dissolution from LCO surface, corresponding to the identified CoF_2^+ species on LCO surface.

Combining the above results, the progressively densified CEI of Z-LCO by regulating surface Zr-O deposits (ZrO_2 and Li_2ZrO_3) is revealed (**Figure 5f**). For Z-LCO, the interface reaction is significantly regulated by the surface Zr-O deposits. First, the ultra-stable surface of Z-LCO can effectively inhibit the organic solvent's decomposition; second, the inescapable existence of H^+ in the initial electrolyte can react with the Zr-O deposits and promote the decomposition of $LiPF_6$ salt, producing plenty of LiF and $Li_xPO_yF_z$ components enriching on the surface and making Zr-O species progressively translate into the Zr-O-F species (ZrO_xF_y and $Li_2ZrO_xF_y$) during initial cycles; third, the densification of CEI can be attributed to chemical reaction between ZrO_xF_y and LiF, producing more beneficial $Li_2ZrO_xF_y$ and Li_2ZrF_6, to reinforce the toughness and conductivity of CEI layer.[43] As a result, the CEI of Z-LCO after long-term cycles shows the uniform, dense and inorganic-rich characters, containing LiF, $Li_xPF_yO_z$, Zr-

O-F and Zr-F species, thus exhibits the better stability and Li^+ transport kinetics. As a contrast, for Z-LCO-Ar with sparse and uneven surface Zr-O deposits and LCO without surface modification, the HF corrosion is difficult to avoid, and the CEI contains more Co-F and organic species, thus can hardly provide good protectiveness on LCO surface structure.

2.5 Cracks' suppression and structure stabilization

As discussed above, the interface reactions are greatly regulated by the Zr-O deposits and RS layer on surface of Z-LCO, forming a robust CEI to stabilize the surface structure. Besides the surface stabilization, the regulated interface reactions can further affect the reversibility of the bulk phase transition of Z-LCO, thus leading to the reduced cracks' formation in LCO particles. Our previous studies have pointed out, the uneven Li^+ extraction from the LCO surface can lead to the irreversible O3/H1-3 phase transition with unrecoverable sliding of Co-O slabs and stress accumulation, finally result in the surface step-like degradation (SSD), i.e. some fresh Co-O slabs on LCO surface are exposed to electrolyte, causing a series of issues including the cracks formation, lattice oxygen loss, and side reaction, etc.[44-46] Thus, tuning surface chemistry of LCO can benefit for the stable and reversible transport of Li^+ ions in LCO particles, which can also efficiently suppress the cracks' formation and maintain the structural integrity upon high voltage operations.

The bulk phase transitions of LCO, Z-LCO-Ar and Z-LCO are further analyzed via *in-situ* XRD tests and dQ/dV curves. **Figure 6a,b and Figure S38a (Supporting Information)** show the *in-situ* XRD results in the initial two cycles, in which the variation of characteristic peaks of LCO are identified, including the (003), (101) and (104) peaks. Comparing with LCO, the more enhanced O3/H1-3 phase transitions occur for Z-LCO-Ar and Z-LCO, showing the obvious characteristic peaks of H1-3 phase (hybrid-phase of O1 and O3), locating at the 2theta of 19.6, 37.0, and 44.0 degrees, respectively.[47-48] The enhanced O3/H1-3 phase transitions are attributed to the increased surface Li^+ transport kinetics of Z-LCO and Z-LCO-Ar due to the surface modulation, leading to more Li^+ extraction from bulk LCO at high voltage.

To further determine the degree of O3/H1-3 phase transition qualitatively, the relative content of O3', O3'/H1-3, H1-3 phases are fitted and analyzed (upon charging to 4.6 V), and the peakdifferentiating and imitating results are shown in **Figure 6c,d and Figure S38b (Supporting Information)**. The O3'/H1-3 phase refers to the intergrowth of O3' and H1-3 phases, which can also be understood as the hybrid-phase with relatively more O3 phase and few O1 phase.[10, 47-49] Besides, for Z-LCO, it shows high content of H1-3 phase (18% in 1st cycle, 24% in 2nd cycle), which is higher than that of Z-LCO-Ar and LCO, indicating a more enhanced O3/H1-3 phase transition of Z-LCO.[50]

The reversibility of bulk phase transitions of LCO, Z-LCO-Ar and Z-LCO are further illustrated by the dQ/dV curves during long-term cycles in 3-4.6 V (**Figure 6e,f; Figure S38c, Supporting Information**). For dQ/dV curves, the peaks locating at 3.9 V and 4.55 V represent the O3/O3' and O3'/H1-3 phase transitions, respectively. For LCO, both the O3/O3' and O3'/H1-3 phase transitions reduce upon cycles, indicating the irreversible phase transitions due to the progressive structure collapse upon cycle. For Z-LCO-Ar, the reversibility of phase transitions enhance, but the polarization of phase transitions gains gradually due to the deteriorated surface structure. Thus, it shows an impedance-increased and reversible phase transitions. For Z-LCO, it shows the enhanced and highly reversible phase transitions upon cycles, mainly attributing to the reinforced CEI layer and well-maintained surface/bulk structures. The XRD patterns of LCO, Z-LCO-Ar and Z-LCO electrodes after 500 cycles are further applied to confirm the results above (**Figure 6g; Figure S38d, Supporting Information**). As observed, the (003) peaks of Z-LCO remain nearly unchanged in 500 cycles, while for Z-LCO-Ar and LCO, obvious (003) peak shifts are observed.

The morphological and structural changes of LCO, Z-LCO-Ar and Z-LCO are directly analyzed by SEM and HRTEM. In **Figure S39a,b (Supporting Information)**, obvious cracks exist in LCO and Z-LCO-Ar after 500 cycles, which is consistent with the cross-sectional SEM images (**Figure S39d,e, Supporting Information**). In contrast, the particle integrity is well-preserved for Z-LCO, without any cracks in the bulk, and the CEI layer is fully covered on the surface (**Figure S39c,f, Supporting Information**), indicating the stabilized bulk structure of Z-LCO. Besides, the surface structure variations after 500 cycles are further characterized. It can be observed that, for LCO, the surface region is severely damaged with obvious cracks (**Figure 7a**), and for Z-LCO-Ar, some micro-cracks are clearly observed in the surface region (**Figure S40a, Supporting Information**). In contrast, for Z-LCO, the surface exhibits a smooth character, and without any micro-cracks (**Figure 7c**). Combining the TEM and correlated FFT results, in **Figure 7b**, for surface of LCO, it exhibits not only the RS phase in the surface region, but also shows the spinel phase nearby the micro-cracks, indicating the plenty of O loss and Co dissolution from surface of LCO in 500 cycles. For Z-LCO-Ar (**Figure S40b, Supporting Information**), comparing with the pristine surface, the surface RS phase layer becomes obviously thicker in 500 cycles, with a thickness of about 30 nm, and the subsurface region also exhibits the spinel phase layer, instead of the pristine layered phase. This result demonstrates the unavoidable Co/O loss from surface of Z-LCO-Ar upon cycle, which may be attributed to the poor protectiveness of CEI. For Z-LCO, after 500 cycles, the surface RS layer still remains a thickness of about 5 nm, and the subsurface region shows the layered structure (**Figure 7d**), attributing to the reinforced CEI induced by the surface Zr-O deposits. And the reason of unclear CEI on surface of Z-LCO in **Figure 7c,d** is due to the FIB milling process in the preparation of TEM samples.

Combining the above, the progressively reinforced CEI is vital for the enhanced structure stability of Z-LCO at 4.6/4.65 V, as illustrated in **Figure 8**. For LCO, the fragile surface is rapidly deteriorated due to the severe HF corrosion and Co/O loss issues, which cause the irreversible bulk phase transition and cracks formation, and result in the rapid capacity decay at high voltage. For Z-LCO-Ar (**Figure S40c, Supporting Information**), although the surface structure is modulated by forming a thick surface RS layer, the CEI formed on the surface of Z-LCO-Ar is not robust enough to protect it from Co/O loss during long-term cycles, leading to the further generation of RS phases and spinel phase on the surface with a high R_{ct} value and cracks formation. As a result, Z-LCO-Ar presents the unsatisfactory cycle stability. For Z-LCO, not only the CEI is progressively reinforced and densified due to the existence of surface Zr-O deposits, but also the surface structure is modulated by forming a thin surface RS layer. As a result, the enhanced but more reversible bulk phase transition is achieved, and the surface structure is well-preserved even after long-term cycles.

3 Conclusion

In summary, this work reveals a novel Zr-O deposits on surface of Z-LCO as the basis of robust

CEI formation, and emphasizes the significance of protective CEI for LCO upon high voltage operations (≥4.6 V). Upon cycle, these Zr-O deposits (ZrO_2 and Li_2ZrO_3), can promote the decomposition of $LiPF_6$ salt, and progressively convert to the highly dispersed Zr-O-F species (ZrO_xF_y and $Li_2ZrO_xF_y$), accompanying with the densification of CEI layer, which greatly reinforces the toughness and conductivity of CEI containing LiF/$Li_xPF_yO_z$/Zr-O-F/Zr-F inorganic species. The stabilized interface structure effectively reduce the surface oxidative activity, ensure the enhanced and reversible O3/H1-3 phase transition, and maintain the surface structure without cracks' formation. As a result, the Z-LCO||Li cells exhibit a high capacity retention of 84.2% after 1000 cycles in 3-4.65 V, 80.9% after 1500 cycles in 3-4.6 V, and a high rate capacity of 160 mA h g^{-1} at 16 C (1 C = 200 mA g^{-1}), which is among the best reported performances for high-voltage LCO.

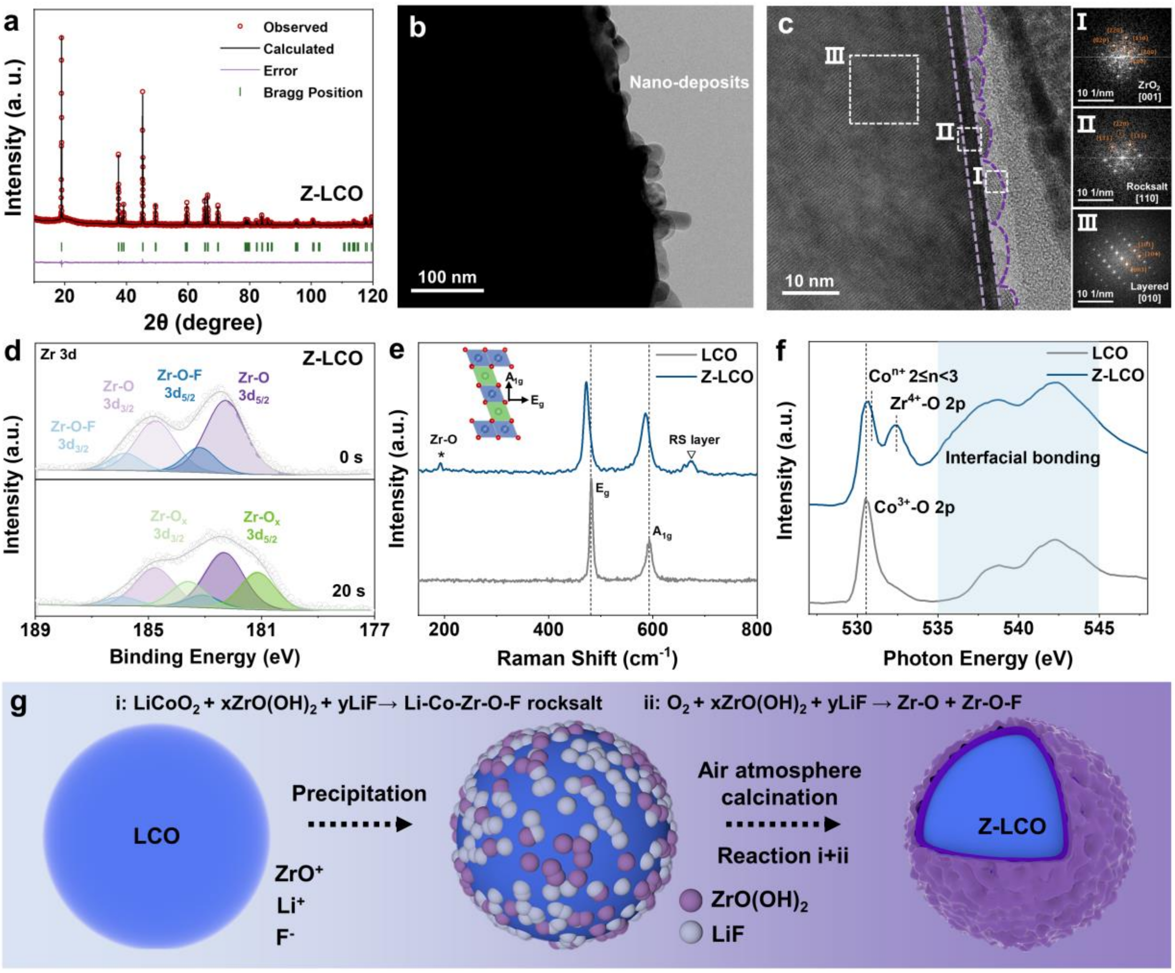

Figure 1. Structural characterizations of Z-LCO. a) XRD and Rietveld refinement pattern of Z-LCO. b) HRTEM image of Z-LCO (entire particles without FIB milling treatment). c) HRTEM image and corresponding fast Fourier transform (FFT) results of Z-LCO after FIB milling treatment. d) The Zr 3d XPS patterns of Z-LCO. e) The Raman spectra of LCO and Z-LCO. f) O K-edge spectra of TEY mode from sXAS measurements of LCO and Z-LCO. g) The schematic diagram of synthesis process for Z-LCO.

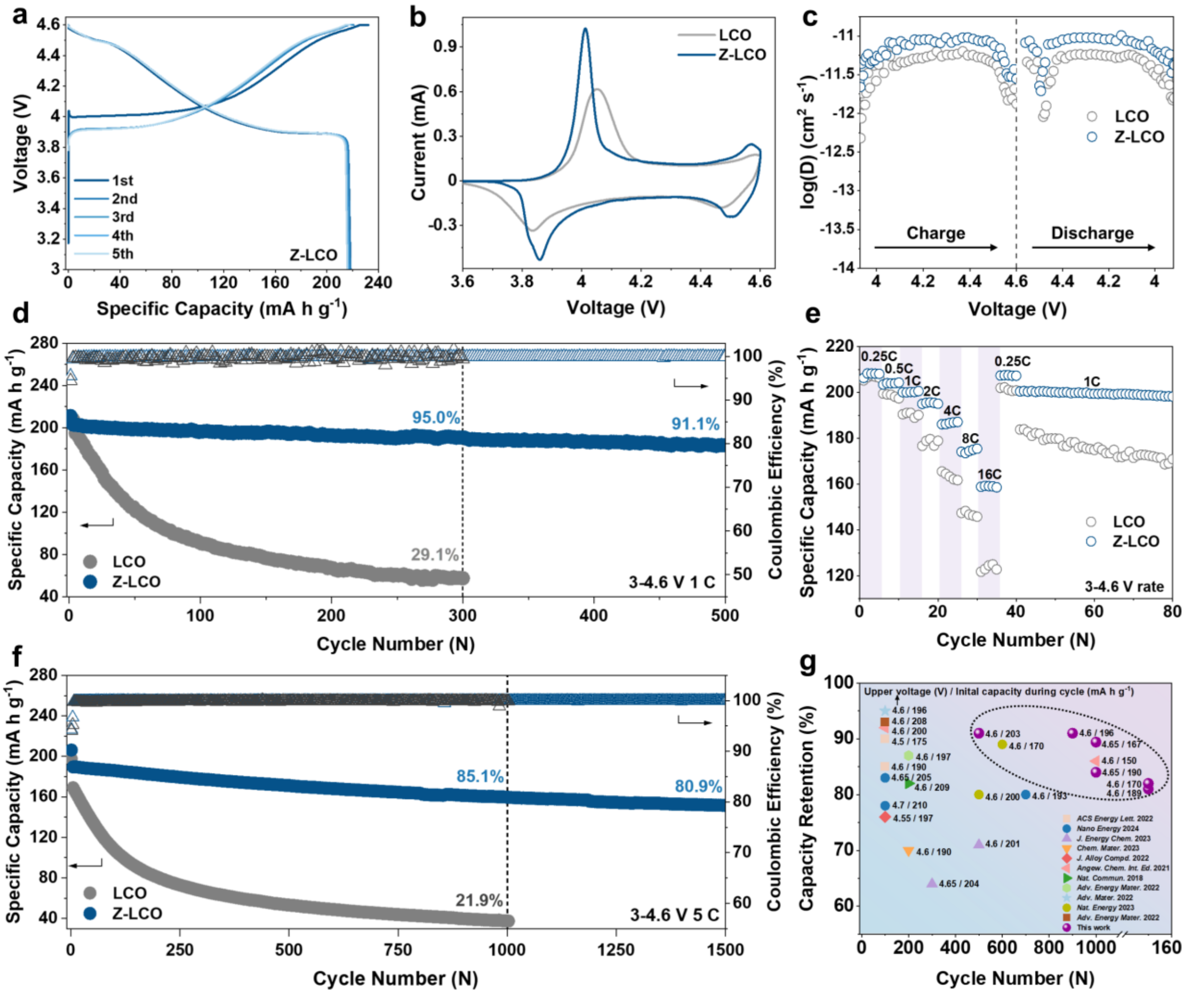

Figure 2. Electrochemical performance of LCO||Li cells and Z-LCO||Li cells at 25℃. a) Charge-discharge curves of Z-LCO within a voltage range of 3-4.6 V at 0.2 C (upon a constant current 0.2 C plus constant voltage charging 0.02 C). b) CV tests of LCO and Z-LCO within a voltage range of 3-4.6 V at a constant voltage scanning of 0.2 mV s^{-1}. c) GITT tests of LCO and Z-LCO within a voltage range of 3-4.6 V. d) Cycle performance of LCO||Li cells and Z-LCO||Li cells within a voltage range of 3-4.6 V at 1 C. e) Rate performance of LCO||Li cells and Z-LCO||Li cells within a voltage range of 3-4.6 V. f) Cycle performance of LCO||Li cells and Z-LCO||Li cells within a voltage range of 3-4.6 V at 5 C. g) Electrochemical performance comparison of recently reported LCO with surface modification.

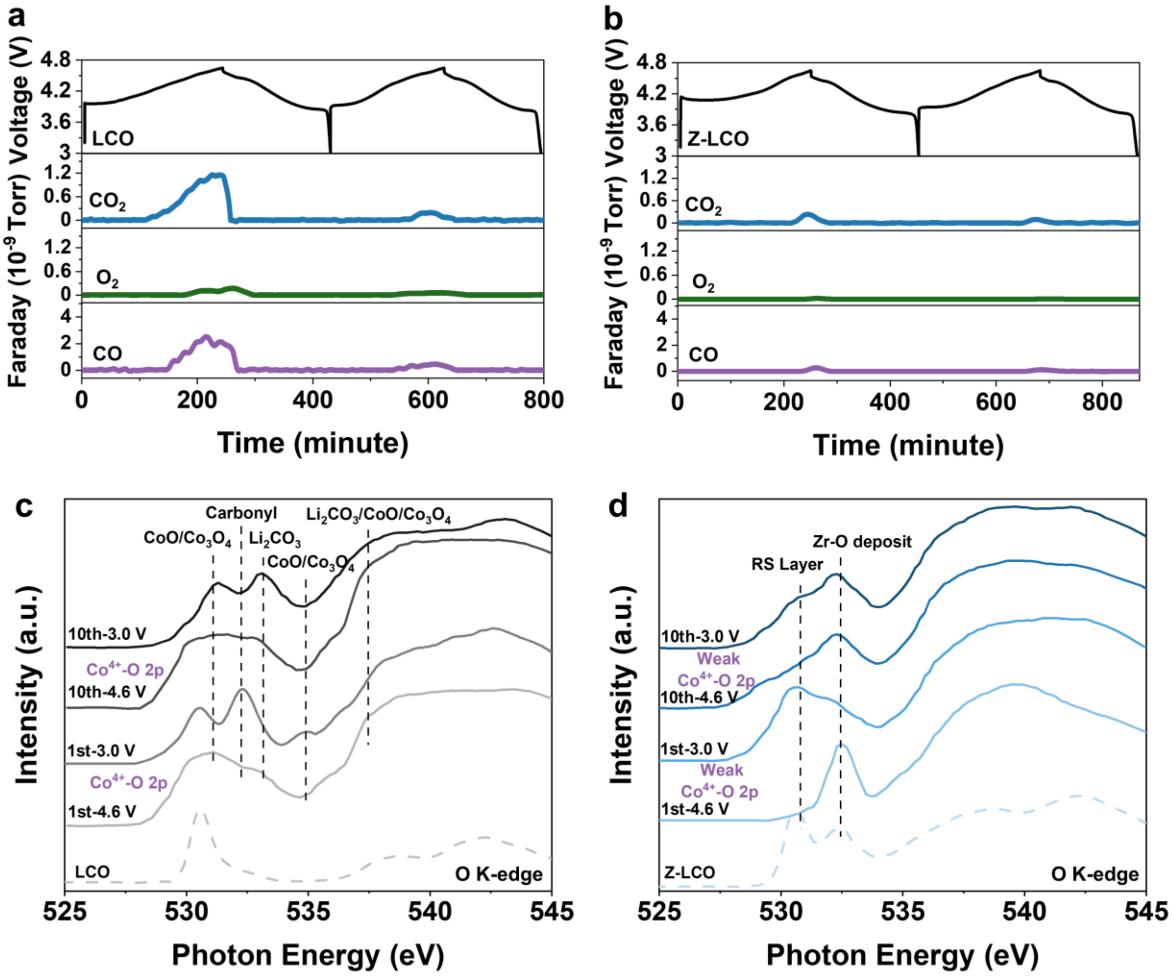

Figure 3. Characterizations of LCO/electrolyte interface side reaction during the initial few cycles. The *in-situ* DEMS tests of a) LCO and b) Z-LCO within a voltage range of 3-4.6 V. O K-edge spectra of TEY mode from sXAS measurements of c) LCO and d) Z-LCO during 1st and 10th cycle within a voltage range of 3-4.6 V.

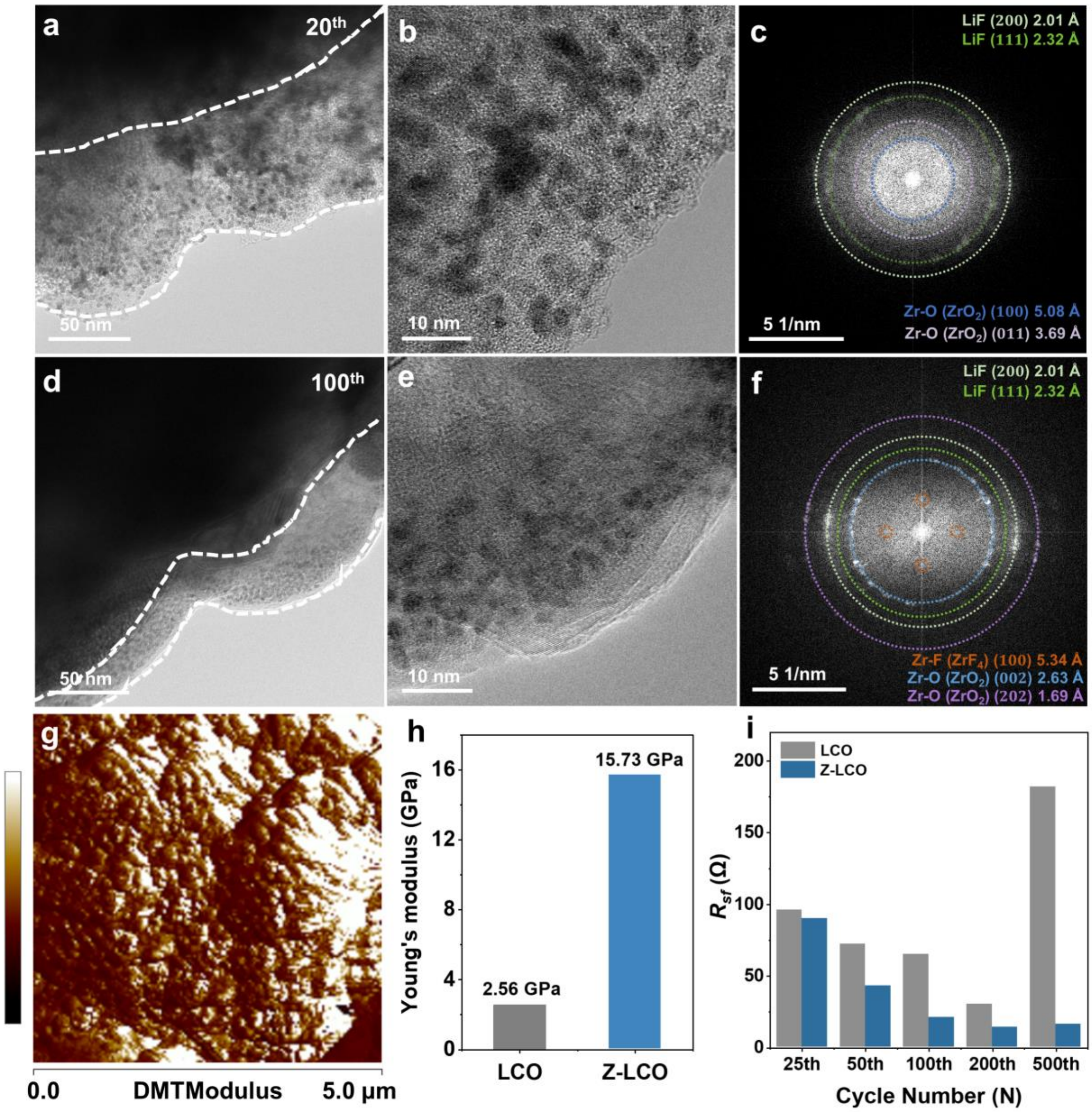

Figure 4. The evolution process of Z-LCO CEI layer. a) Cryo-TEM characterizations of Z-LCO CEI layer, corresponding b) large-scale images and c) FFT analysis after 20 cycles within a voltage range of 3-4.6 V at 1 C. d) Cryo-TEM characterizations of Z-LCO CEI layer, corresponding e) large-scale images and f) FFT analysis after 100 cycles within a voltage range of 3-4.6 V at 1 C. g) The mechanical properties of Z-LCO CEI layer after 100 cycles measured by AFM and the corresponding h) average Young's modulus values of Z-LCO and LCO. i) The fitting results of EIS measurements of Z-LCO||Li cells and LCO||Li cells after different cycles within a voltage range of 3-4.6 V at 1 C.

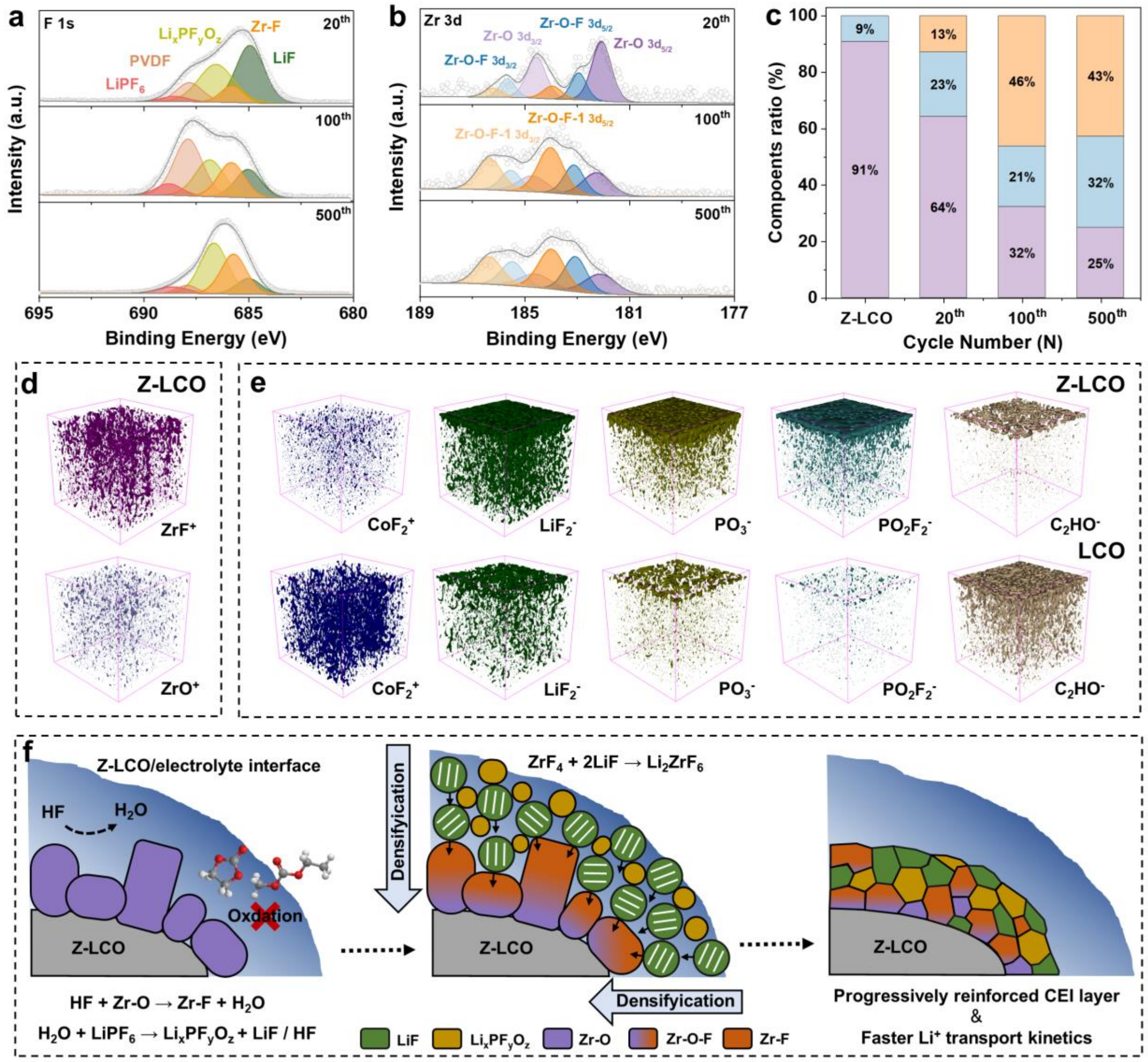

Figure 5. The mechanism of progressively reinforced CEI layer of Z-LCO. a) F 1s and b) Zr 3d XPS patterns of Z-LCO after different cycles within a voltage range of 3-4.6 V at 1 C. c) The content variation of Zr-O/Zr-O-F species on Z-LCO after different cycles within a voltage range of 3-4.6 V at 1 C (calculated by the Zr 3d XPS results). d) The 3D reconstruction of ZrF^+ and ZrO^+ secondary-ion fragments in CEI of Z-LCO and e) the comparison of CoF_2^+, LiF_2^-, PO_3^-, $PO_2F_2^-$ and C_2HO^- species in CEI of Z-LCO and LCO after 100 cycles within a voltage range of 3-4.6 V at 1 C. f) The schematic diagram of the mechanism of progressively densified CEI layer for Z-LCO.

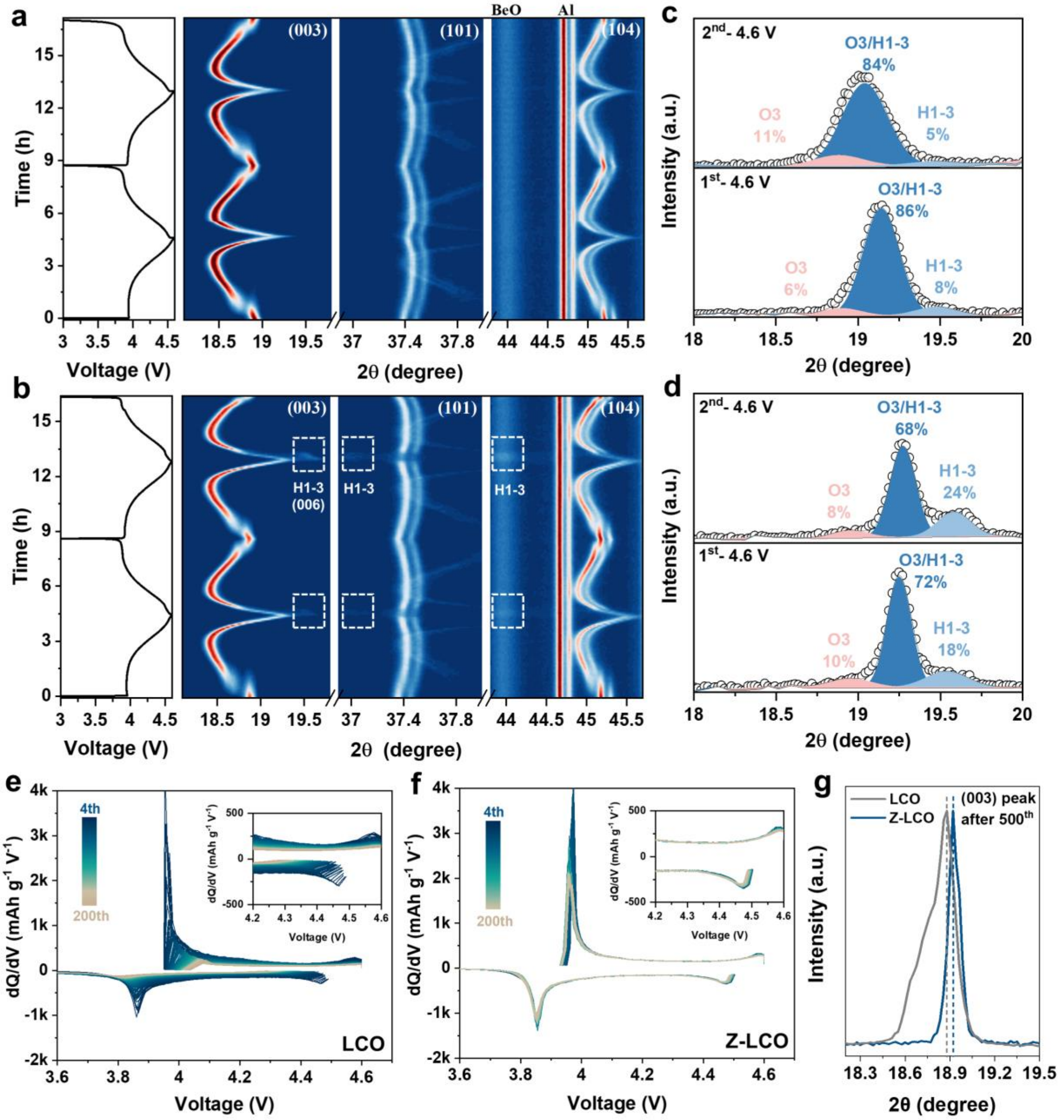

Figure 6. The differences of phase transition between LCO and Z-LCO. a,b) The *in-situ* XRD measurements of LCO and Z-LCO during the initial two cycles within a voltage range of 3-4.6 V at 0.25 C and c,d) the main peak resolving at 4.6 V charged state. The dQ/dV curves during 200 cycles of e) LCO||Li cells and f) Z-LCO||Li cells within a voltage range of 3-4.6 V at 1 C. g) The comparison of (003) peak position in XRD patterns of LCO and Z-LCO after 500 cycles within a voltage range of 3-4.6 V at 1 C.

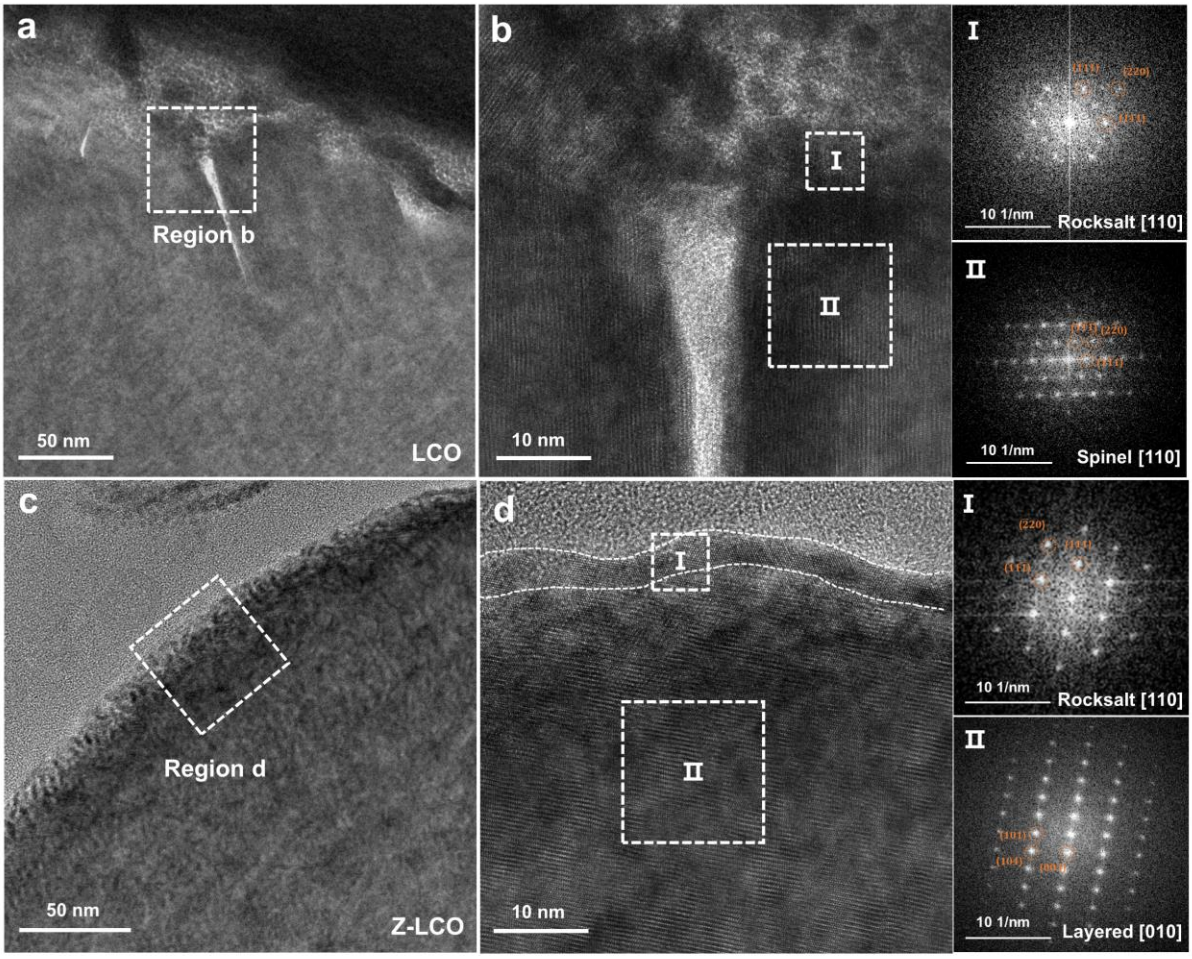

Figure 7. Long-term structure characterizations. The HRTEM of a,b) LCO, c,d) Z-LCO and corresponding FFT results after 500 cycles within a voltage range of 3-4.6 V at 1 C.

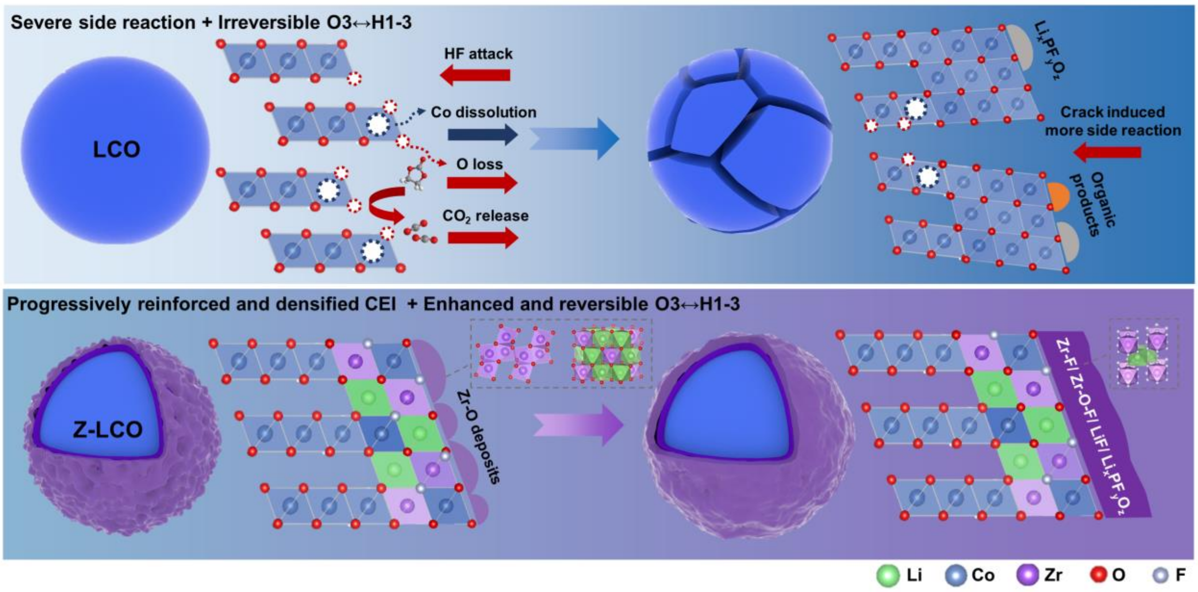

Figure 8. Schematic diagram of stabilization of Z-LCO under high voltage operation.

Acknowledgement

This work is financially supported by the International joint Research Center for Electric Vehicle Power Battery and Materials (No.2015B01015), the Basic and Applied Basic Research Foundation of Guangdong Province (No.2021B1515130002), Guangdong Key Laboratory of Design and calculation of New Energy Materials (No. 2017B030301013), and Shenzhen Key Laboratory of New Energy Resources Genome Preparation and Testing (No. ZDSYS201707281026184).

Conflicts of interest

The authors declare no competing interests.

Reference

[1] J. Li, C. Lin, M. Weng, Y. Qiu, P. Chen, K. Yang, W. Huang, Y. Hong, J. Li, M. Zhang, C. Dong, W. Zhao, Z. Xu, X. Wang, K. Xu, J. Sun, F. Pan, *Nat. Nanotechnol.* **2021**, *16*, 599-605.

[2] C. Lin, J. Li, Z. W. Yin, W. Huang, Q. Zhao, Q. Weng, Q. Liu, J. Sun, G. Chen, F. Pan, *Adv. Mater.* **2023**, *36*, 2307404.

[3] Y. Huang, *Interdiscip. Mater.* **2022**, *1*, 323-329.

[4] M. Cai, Y. Dong, M. Xie, W. Dong, C. Dong, P. Dai, H. Zhang, X. Wang, X. Sun, S. Zhang, M. Yoon, H. Xu, Y. Ge, J. Li, F. Huang, *Nat. Energy* **2023**, *8*, 159-168.

[5] B. L. D. Rinkel, D. S. Hall, I. Temprano, C. P. Grey, *JACS* **2020**, *142*, 15058-15074.

[6] Y. Zhang, Y. Katayama, R. Tatara, L. Giordano, Y. Yu, D. Fraggedakis, J. G. Sun, F. Maglia, R. Jung, M. Z. Bazant, Y. Shao-Horn, *Energy Environ. Sci.* **2020**, *13*, 183-199.

[7] Y. Yan, S. Weng, A. Fu, H. Zhang, J. Chen, Q. Zheng, B. Zhang, S. Zhou, H. Yan, C.-W. Wang, Y. Tang, H. Luo, B.-W. Mao, J. Zheng, X. Wang, Y. Qiao, Y. Yang, S.-G. Sun, *ACS Energy Lett.* **2022**, *7*, 2677-2684.

[8] W. Ding, H. Ren, Z. Li, M. Shang, Y. Song, W. Zhao, L. Chang, T. Pang, S. Xu, H. Yi, L. Zhou, H. Lin, Q. Zhao, F. Pan, *Adv. Energy Mater.* **2024**, *14*, 2303926.

[9] Z. Li, H. Yi, W. Ding, H. Ren, Y. Du, M. Shang, W. Zhao, H. Chen, L. Zhou, H. Lin, Q. Zhao, F. Pan, *Adv. Funct. Mater.* **2023**, *34*, 2312837.

[10] Z. Wu, G. Zeng, J. Yin, C.-L. Chiang, Q. Zhang, B. Zhang, J. Chen, Y. Yan, Y. Tang, H. Zhang, S. Zhou, Q. Wang, X. Kuai, Y.-G. Lin, L. Gu, Y. Qiao, S.-G. Sun, *ACS Energy Lett.* **2023**, *8*, 4806-4817.

[11] P. Bai, X. Ji, J. Zhang, W. Zhang, S. Hou, H. Su, M. Li, T. Deng, L. Cao, S. Liu, X. He, Y. Xu, C. Wang, *Angew. Chem. Int. Ed.* **2022**, *61*, e202202731.

[12] S. Tan, Z. Shadike, J. Li, X. Wang, Y. Yang, R. Lin, A. Cresce, J. Hu, A. Hunt, I. Waluyo, L. Ma, F. Monaco, P. Cloetens, J. Xiao, Y. Liu, X.-Q. Yang, K. Xu, E. Hu, *Nat. Energy* **2022**, *7*, 484-494.

[13] D. Wu, C. Zhu, H. Wang, J. Huang, G. Jiang, Y. Yang, G. Yang, D. Tang, J. Ma, *Angew. Chem. Int. Ed.* **2024**, *63*, e202315608.

[14] J. Liu, B. Yuan, N. He, L. Dong, D. Chen, S. Zhong, Y. Ji, J. Han, C. Yang, Y. Liu, W. He, *Energy Environ. Sci.* **2023**, *16*, 1024-1034.

[15] C. Yang, X. Liao, X. Zhou, C. Sun, R. Qu, J. Han, Y. Zhao, L. Wang, Y. You, J. Lu, *Adv. Mater.* **2023**, *35*.

[16] Z. Li, H. Yi, H. Ren, J. Fang, Y. Du, W. Zhao, H. Chen, Q. Zhao, F. Pan, *Adv. Funct. Mater.* **2023**, *33*, 2307913.

[17] J. Liu, J. Wang, Y. Ni, J. Liu, Y. Zhang, Y. Lu, Z. Yan, K. Zhang, Q. Zhao, F. Cheng, J. Chen, *Angew. Chem. Int. Ed.* **2022**, *61*, e202207000.

[18] W. Li, D. Cheng, R. Shimizu, Y. Li, W. Yao, G. Raghavendran, M. Zhang, Y. S. Meng, *Energy Storage Mater.* **2022**, *49*, 77-84.

[19] H. Ren, W. Zhao, H. Yi, Z. Chen, H. Ji, Q. Jun, W. Ding, Z. Li, M. Shang, J. Fang, K. Li, M. Zhang, S. Li, Q. Zhao, F. Pan, *Adv. Funct. Mater.* **2023**, *33*, 2302622.

[20] A. Yano, M. Hirayama, R. Kanno, *Electrochemistry* **2019**, *87*, 234-241.

[21] J. L. Tebbe, A. M. Holder, C. B. Musgrave, *ACS Appl. Mater. Interfaces* **2015**, *7*, 24265-24278.

[22] Z. H. Chen, J. R. Dahn, *Electrochem. Solid State Lett.* **2003**, *6*, A221-A224.

[23] C. G. Pantano, R. K. Brow, *J. Am. Ceram. Soc.* **2005**, *71*, 577-581.

[24] J. I. Hata, M. Hirayama, K. Suzuki, N. Dupré, D. Guyomard, R. Kanno, *Batteries Supercaps* **2019**, *2*, 454-463.

[25] N. Qin, Q. Gan, Z. Zhuang, Y. Wang, Y. Li, Z. Li, I. Hussain, C. Zeng, G. Liu, Y. Bai, K. Zhang, Z. Lu, *Adv. Energy Mater.* **2022**, *12*, 2201549.

[26] J. L. You, G. C. Jiang, S. H. Yang, J. C. Ma, K. D. Xu, *Chinese Phys. Lett.* **2001**, *18*, 991-993.

[27] L. F. Edge, D. G. Schlom, S. Stemmer, G. Lucovsky, J. Luning, *Radiat. Phys. Chem.* **2006**, *75*, 1608-1612.

[28] G. Lucovsky, C. L. Hinkle, C. C. Fulton, N. A. Stoute, H. Seo, J. Lüning, *Radiat. Phys. Chem.* **2006**, *75*, 2097-2101.

[29] J. Chen, H. Chen, S. Zhang, A. Dai, T. Li, Y. Mei, L. Ni, X. Gao, W. Deng, L. Yu, G. Zou, H. Hou, M. Dahbi, W. Xu, J. Wen, J. Alami, T. Liu, K. Amine, X. Ji, *Adv. Mater.* **2022**, *34*, 2204845.

[30] J. Zheng, J. Lu, K. Amine, F. Pan, *Nano Energy* **2017**, *33*, 497-507.

[31] X.-H. Long, Y.-R. Wu, N. Zhang, P.-F. Yu, X.-F. Feng, S. Zheng, J.-M. Fu, X.-S. Liu, N. Liu, M. Wang, L.-M. Xu, J.-M. Chen, J.-M. Lee, *Chinese Phys. B* **2018**, *27*, 107802.

[32] C. Yogi, D. Takamatsu, K. Yamanaka, H. Arai, Y. Uchimoto, K. Kojima, I. Watanabe, T. Ohta, Z. Ogumi, *J. Power Sources* **2014**, *248*, 994-999.

[33] H. W. Zhi Zhu, Yao Li, Rui Gao, Xianghui Xiao, Qipeng Yu, Chao Wang, Iradwikanari Waluyo, Jiaxin Ding, Adrian Hunt, and Ju Li, *Adv. Mater.* **2020**, *32*, 2005182.

[34] Y. Li, Y. Li, A. Pei, K. Yan, Y. Sun, C.-L. Wu, L.-M. Joubert, R. Chin, A. L. Koh, Y. Yu, J. Perrino, B. Butz, S. Chu, Y. Cui, *SCIENCE* **2017**, *358*, 506-510.

[35] Z. Zhang, J. Yang, W. Huang, H. Wang, W. Zhou, Y. Li, Y. Li, J. Xu, W. Huang, W. Chiu, Y. Cui, *Matter* **2021**, *4*, 302-312.

[36] O. Sheng, J. Zheng, Z. Ju, C. Jin, Y. Wang, M. Chen, J. Nai, T. Liu, W. Zhang, Y. Liu, X. Tao, *Adv. Mater.* **2020**, *32*, 2000223.

[37] Z. S. Wu, L. Xue, W. Ren, F. Li, L. Wen, H. M. Cheng, *Adv. Funct. Mater.* **2012**, *22*, 3290-3297.

[38] A. Yano, M. Shikano, A. Ueda, H. Sakaebe, Z. Ogumi, *J. Electrochem. Soc.* **2016**, *164*, A6116-A6122.

[39] Y. Lu, C.-Z. Zhao, J.-Q. Huang, Q. Zhang, *Joule* **2022**, *6*, 1172-1198.

[40] G. Zheng, S. Xue, Y. Li, S. Chen, J. Qiu, Y. Ji, M. Liu, L. Yang, *Nano Energy* **2024**, *125*, 109617.

[41] T. H. Wan, M. Saccoccio, C. Chen, F. Ciucci, *Electrochim. Acta* **2015**, *184*, 483-499.

[42] R. Xu, C. Yan, Y. Xiao, M. Zhao, H. Yuan, J.-Q. Huang, *Energy Storage Mater.* **2020**, *28*, 401-406.

[43] J. Moon, S. Thiangtham, R. Zheng, S. Liu, C. Chokradjaroen, Y. Sawada, N. Saito, *Journal of Energy and Power Technology* **2023**, *05*, 1-23.

[44] X. Wang, H. Ren, Y. Du, Z. Li, W. Zhao, H. Ji, H. Yi, Q. Pan, J. Liu, Z. Lou, L. Zhou, F. Pan, Q. Zhao, *Nano Energy* **2024**, *125*, 109537.

[45] H. Yi, Y. Du, J. Fang, Z. Li, H. Ren, W. Zhao, H. Chen, L. Zhou, Q. Zhao, F. Pan, *ACS Appl. Mater. Interfaces* **2023**, *15*, 42667-42675.

[46] M. Shang, H. Ren, W. Zhao, Z. Li, J. Fang, H. Chen, W. Fan, F. Pan, Q. Zhao, *ACS Nano* **2024**, *18*, 16982-16993.

[47] M. Hirooka, T. Sekiya, Y. Omomo, M. Yamada, H. Katayama, T. Okumura, Y. Yamada, K. Ariyoshi, *J. Power Sources* **2020**, *463*, 228127.

[48] A. Van der Ven, M. K. Aydinol, G. Ceder, *J. Electrochem. Soc.* **1998**, *145*, 2149-2155.

[49] A. Yano, N. Taguchi, H. Kanzaki, M. Shikano, H. Sakaebe, *J. Electrochem. Soc.* **2021**, *168*.

[50] W. Huang, J. Li, Q. Zhao, S. Li, M. Ge, J. Fang, Z. Chen, L. Yu, X. Huang, W. Zhao, X. Huang, G. Ren, N. Zhang, L. He, J. Wen, W. Yang, M. Zhang, T. Liu, K. Amine, F. Pan, *Adv. Mater.* **2024**, 36, 2405519.